

PointNSP: Autoregressive 3D Point Cloud Generation with Next-Scale Level-of-Detail Prediction

Ziqiao Meng¹ Qichao Wang² Zhiyang Dou³ Zixing Song⁴ Zhipeng Zhou²
Irwin King⁵ Peilin Zhao⁶

¹National University of Singapore ²Nanyang Technological University
³University of Hong Kong ⁴University of Cambridge
⁵The Chinese University of Hong Kong ⁶Shanghai Jiao Tong University

Abstract

Autoregressive point cloud generation has long lagged behind diffusion-based approaches in quality. The performance gap stems from the fact that autoregressive models impose an artificial ordering on inherently unordered point sets, forcing shape generation to proceed as a sequence of local predictions. This sequential bias emphasizes short-range continuity but undermines the model’s capacity to capture long-range dependencies, hindering its ability to enforce global structural properties such as symmetry, consistent topology, and large-scale geometric regularities. Inspired by the level-of-detail (LOD) principle in shape modeling, we propose *PointNSP*, a coarse-to-fine generative framework that preserves global shape structure at low resolutions and progressively refines fine-grained geometry at higher scales through a next-scale prediction paradigm. This multi-scale factorization aligns the autoregressive objective with the permutation-invariant nature of point sets, enabling rich intra-scale interactions while avoiding brittle fixed orderings. Experiments on ShapeNet show that *PointNSP* establishes state-of-the-art (SOTA) generation quality for the first time within the autoregressive paradigm. In addition, it surpasses strong diffusion-based baselines in parameter, training, and inference efficiency. Finally, in dense generation with 8,192 points, *PointNSP*’s advantages become even more pronounced, underscoring its scalability potential.¹

1 Introduction

Point clouds are a fundamental representation of 3D object shapes, describing each object as a collection of points in Euclidean space. They arise naturally from sensors such as LiDAR and laser scanners, offering a compact yet expressive encoding of fine-grained geometric details. Developing powerful generative models for point clouds is key to uncovering the underlying distribution of 3D shapes, with broad applications in shape synthesis, reconstruction, computer-aided design, and perception for robotics and autonomous systems. However, high-fidelity point cloud generation remains challenging due to the irregular and unordered nature of point

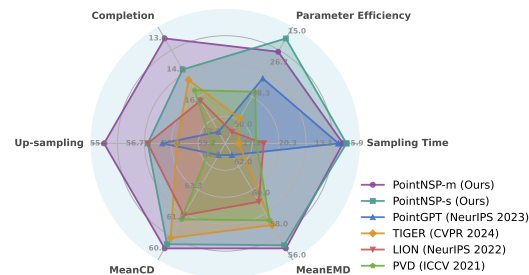


Figure 1: A comprehensive performance comparison between *PointNSP* and recent strong baseline methods across six key metrics.

¹Project Homepage: <https://pointnsp.pages.dev>

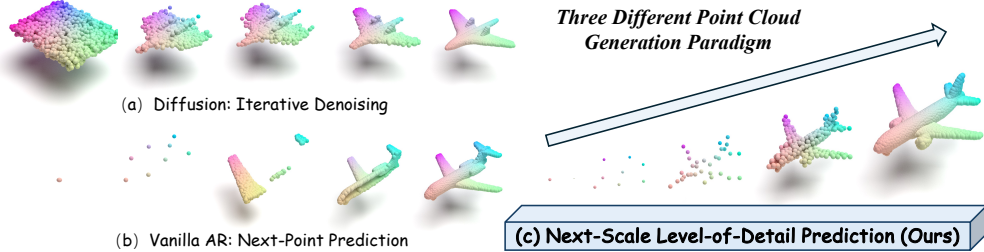


Figure 2: Three types of point cloud generative models: (a) diffusion-based methods that iteratively denoise shapes starting from Gaussian noise; (b) vanilla autoregressive (AR) methods that predict the next point by flattening the 3D shape into a sequence; and (c) our proposed *PointNSP*, which predicts next-scale level-of-detail in a coarse-to-fine manner.

sets [40, 41, 69]. Unlike images or sequences, point clouds have no inherent ordering—permuting the points leaves the shape unchanged—making naive order-dependent methods poorly suited for their generation and analysis.

In recent years, diffusion-based methods [74, 70, 48] have become the dominant paradigm for 3D point cloud generation, delivering strong results. However, their Markovian assumption overlooks global context, often leading to incoherent shapes. Moreover, diffusion models are computationally costly, as generating high-quality samples typically requires hundreds to thousands of denoising steps—a burden that grows prohibitive when producing dense point clouds. By contrast, autoregressive (AR) models condition on the full history, enabling explicit modeling of long-range dependencies while generally offering faster sampling. Unlike diffusion models, existing AR methods require flattening inherently unordered point clouds into sequences. Point Transformers [72, 63, 64] design specialized architectures for unordered point sets and explore diverse point cloud serialization strategies to improve speed, at the expense of relaxing permutation invariance. PointGrow [54] enforces a sequential order by sorting points along the z -axis. ShapeFormer [65] voxelizes point clouds and flattens codebook embeddings into sequences using a row-major order. PointVQVAE [7] projects patches onto a sphere and arranges them in a spiral sequence to establish a canonical mapping. AutoSDF [35] treats point clouds as randomly permuted sequences of latent variables, while PointGPT [4] leverages Morton code ordering to impose structure on unordered data. Although these approaches yield promising results, they still lag behind state-of-the-art diffusion-based methods [33, 74, 70, 48] in generation quality. This is largely due to the restrictive unidirectional dependencies imposed by fixed sequential orders, which collapse global shape generation into local predictions and inherently violate the fundamental permutation-invariance property. This naturally raises the question: *can we achieve permutation-invariant autoregressive modeling for 3D point cloud generation?*

In this work, we introduce *PointNSP*, a novel autoregressive framework for 3D point cloud generation that preserves global permutation invariance—a key property ensuring that shapes remain independent of point ordering. Inspired by visual autoregressive modeling in 2D image synthesis [57], *PointNSP* follows a coarse-to-fine strategy, progressively refining point clouds from global structures to fine-grained details via next-scale prediction. Unlike prior approaches that predict one point at a time (next-point prediction), *PointNSP* captures multiple levels of detail (LoD) [31] at each step, enabling more effective modeling of both global geometry and local structure. This design offers two key advantages. First, it avoids collapsing 3D structures by eliminating the need to flatten point clouds into 1D sequences: each step corresponds to a full 3D shape at a given LoD, ensuring structural coherence and permutation invariance. Second, compared to diffusion-based methods, *PointNSP* establishes a more structured and efficient generation trajectory, avoiding iterative noise injection and denoising in 3D space. Together, these advances allow *PointNSP* to achieve high generation quality while maintaining strong modeling efficiency. The comparisons across different paradigms are illustrated in Figure 2.

We conduct extensive experiments on the ShapeNet benchmark to validate the effectiveness of *PointNSP* across diverse settings. In the standard single-class scenario, *PointNSP* achieves state-of-the-art (SOTA) **generation quality**, yielding the lowest average Chamfer Distance and Earth Mover’s Distance—setting a new benchmark for autoregressive modeling. Beyond quality, *PointNSP* also demonstrates substantially higher **parameter efficiency**, **training efficiency**, and **sampling**

speed compared to strong diffusion-based baselines. In the more challenging multi-class setting, *PointNSP* maintains SOTA performance, evidencing superior cross-category generalization. Moreover, *PointNSP* significantly outperforms existing approaches on downstream tasks such as partial point cloud completion and upsampling, further highlighting the robustness and versatility of its design. Comparative results across these metrics are presented in Figure 1. When evaluated on denser point clouds with 8192 points, the advantages of *PointNSP* become even more pronounced, particularly in the aforementioned efficiency metrics, underscoring its *scalability potential*.

2 Related Works

Autoregressive Generative Modeling. The core principle of autoregressive generative models is to synthesize outputs sequentially by iteratively generating intermediate segments. This paradigm has achieved remarkable success in discrete language modeling through next-token prediction [39, 37]. Inspired by these advances, researchers have extended autoregressive modeling to other modalities, including images [12, 20, 8], speech [71, 61], and multi-modal data [73, 56]. Although these modalities are often continuous in nature, they are typically transformed into discrete token representations using techniques such as VQ-VAE (VQ) [58] or residual vector quantization (RVQ) [20], with generation performed over the resulting tokens in predefined orders (e.g., raster-scan sequences). To relax the constraint of strict unidirectional dependencies, MaskGIT [3] predicts sets of randomly masked tokens at each step under the control of a scheduler. More recently, VAR [57] redefines the autoregressive paradigm by predicting the next resolution rather than the next token. Within each scale, a bidirectional transformer enables full contextual interaction among tokens, making VAR especially effective for modeling unordered data such as 3D point clouds. Note that while VAR has been applied to 3D mesh generation [21] and 2D image-conditional 3D triplane generation [6], these works differ fundamentally from ours as they operate on different 3D data structures.

Point Cloud Generation. Deep generative models have made significant strides in 3D point cloud generation. For instance, PointFlow [66] captures the latent distribution of point clouds using continuous normalizing flows [49, 14, 5]. Building on this foundation, a series of approaches—including DPM [33], ShapeGF [2], PVD [74], LION [70], TIGER [48], PDT [59]—leverage denoising diffusion probabilistic models [16, 53] to synthesize 3D point clouds through the gradual denoising of input data or latent representations in continuous space. While efforts to improve the sampling efficiency of diffusion models—such as straight flows [26, 28, 62] and ODE-based solvers [52]—have achieved acceleration, these methods often introduce trade-offs that compromise generation quality. In contrast, autoregressive models for 3D point cloud generation [54, 7, 4] have received relatively less attention, historically lagging behind diffusion-based techniques in terms of fidelity. In this work, we reformulate point cloud generation as an iterative upsampling process, establishing a connection with sparse point cloud upsampling approaches [68, 15, 47]. A more comprehensive review of related point cloud upsampling methods is provided in the Appendix F.

3 Method: PointNSP

3.1 Preliminaries: Autoregressive 3D Point Cloud Generation

A point cloud is represented as a set of N points $\mathbf{X} = \{\mathbf{x}_i\}_{i=1}^N$, where each point $\mathbf{x}_i \in \mathbb{R}^3$ corresponds to a 3D coordinate. Prior autoregressive approaches [7, 54, 4] mainly follow the next-point prediction paradigm:

$$p(\mathbf{x}_1, \mathbf{x}_2, \dots, \mathbf{x}_N) = \prod_{i=1}^N p(\mathbf{x}_i | \mathbf{x}_{i-1}, \dots, \mathbf{x}_2, \mathbf{x}_1). \quad (1)$$

Training Eq. 1 requires a sequential classification objective. Each point \mathbf{x}_i is first converted into a discrete integer token q_i via VQ-VAE quantization [58], and the resulting tokens are flattened into a sequence (q_1, \dots, q_N) according to a predefined generation order. Autoregressive modeling is then applied to this discrete sequence following the paradigm in Eq. 1. However, this approach struggles to preserve permutation invariance, since the probability distribution depends on the chosen token ordering and is not invariant to different permutations of the points. In this work, instead of predicting the next point, we propose a novel autoregressive framework that predicts the next-scale level-of-detail

(LoD) of the point cloud \mathbf{X} , while simultaneously preserving the permutation invariance property:

$$p(\pi(\mathbf{x}_1, \dots, \mathbf{x}_N)) = p(\mathbf{x}_1, \dots, \mathbf{x}_N), \quad \forall \pi \in S_N. \quad (2)$$

In general, we construct k different LoDs of \mathbf{X} , forming a coarse-to-fine sequence of global shapes $\mathbf{X}_1, \dots, \mathbf{X}_K$, where each $\mathbf{X}_k \in \mathbb{R}^{s_k \times 3}$ represents a global shape at resolution s_k , obtained by downsampling the original \mathbf{X} . Then, *PointNSP* is designed to learn the following distribution:

$$p(\mathbf{X}_1, \mathbf{X}_2, \dots, \mathbf{X}_K) = \prod_{k=1}^K p(\mathbf{X}_k | \mathbf{X}_{k-1}, \dots, \mathbf{X}_2, \mathbf{X}_1). \quad (3)$$

In this work, we set $s_1 = 1$ (a single starting point) and $s_K = N$ (total number of points). The generation process can be interpreted as an autoregressive upsampling procedure with sequential upsampling rates r_1, r_2, \dots, r_{K-1} , satisfying the relationship $r_{K-1} \times \dots \times r_1 \times s_1 = s_K = N$. Learning Eq. 3 requires a two-stage training process. The first stage involves training multi-scale VQ-VAE tokenizers to progressively reconstruct different LoDs, while the second stage trains the autoregressive transformer over the resulting multi-scale token sequence.

Algorithm 1 Multi-scale VQVAE encoder

- 1: **Input:** 3D point cloud $\mathbf{X} = \{\mathbf{x}_i\}_{i=1}^N$.
- 2: **Hyperparameters:** # scales $\{s_k\}_{k=1}^K$.
- 3: $f = \mathcal{E}(\mathbf{X})$, $Q = []$;
- 4: **for** $k = 1, \dots, K$ **do**
- 5: $\mathbf{X}_k = \text{FPS}(\mathbf{X}, s_k)$
- 6: $q_k = \mathcal{Q}(f_k)$, $f_k = \text{Query}(f, \mathbf{X}_k)$
- 7: $Q = \text{queue_push}(Q, q_k)$
- 8: $\mathbf{z}_k = \text{lookup}(Z, q_k)$
- 9: $\mathbf{z}_k = \text{upsampling}(\mathbf{z}_k, s_K)$
- 10: $f = f - \phi_k(\mathbf{z}_k)$
- 11: **end for**
- 12: **Return:** token sequence Q .

Algorithm 2 Multi-scale VQVAE decoder

- 1: **Input:** token sequence Q .
- 2: **Hyperparameters:** # scales $\{s_k\}_{k=1}^K$.
- 3: $\hat{f} = 0$
- 4: **for** $k = 1, \dots, K$ **do**
- 5: $q_k = \text{queue_pop}(Q)$
- 6: $\mathbf{z}_k = \text{lookup}(Z, q_k)$
- 7: $\mathbf{z}_k = \text{upsampling}(\mathbf{z}_k, s_K)$
- 8: $\hat{f} = \hat{f} + \phi_k(\mathbf{z}_k)$
- 9: **end for**
- 10: $\hat{\mathbf{X}} = \mathcal{D}(\hat{f})$
- 11: **Return:** reconstructed point cloud $\hat{\mathbf{X}}$

3.2 Multi-Scale LoD Representation

Sampling Multi-Scale LoD Sequence. To obtain $\mathbf{X}_1, \dots, \mathbf{X}_K$, we employ the Farthest Point Sampling (FPS) [11] algorithm to downsample the original point cloud \mathbf{X} . FPS offers two key advantages. First, it is permutation-invariant: point selection depends solely on spatial locations (geometric distances) rather than the order of points in the input array. The stochasticity of the downsampled point cloud arises only from the choice of the initial point, not from the input ordering. Second, FPS operates directly on the original point cloud, enabling straightforward querying of specific point embeddings via stored indices. Importantly, we do not fix the initial starting point of FPS, so the sampled points in \mathbf{X}_k vary during training. This inherent stochasticity enhances model generalization, effectively serving as a form of data augmentation at each scale. Note that $\mathbf{X}_1, \dots, \mathbf{X}_K$ are all obtained directly from the original point cloud \mathbf{X} , i.e., $\mathbf{X}_k = \text{FPS}(\mathbf{X})$ for each scale k , rather than using an iterative downsampling strategy such as $\mathbf{X}_k = \text{FPS}^k(\mathbf{X})$ adopted in 2D image VAR [57], where FPS^k denotes a nested operation with k loops. Directly sampling points from \mathbf{X} in this way increases the shape coverage at each scale of the LoD.

Multi-Scale Feature Extraction. For the encoder to obtain point features $f \in \mathbb{R}^{N \times 3}$ from the point cloud \mathbf{X} , any permutation-equivariant network $\text{NN}(\cdot)$ is applicable: the per-point features reorder consistently with any permutation of the input points, i.e., $\pi(\text{NN}(\mathbf{x}_1, \dots, \mathbf{x}_N)) = \text{NN}(\pi(\mathbf{x}_1, \dots, \mathbf{x}_N))$ for any permutation π . Therefore, permutation-equivariant architectures such as PointNet [40], PointNet++ [41], PointNeXt [43] and PVCNN [29] are all applicable. To construct the multi-scale representations, we extract latent features $f_1 \in \mathbb{R}^{s_1 \times d}, \dots, f_K \in \mathbb{R}^{s_K \times d}$ in a residual querying manner: each \mathbf{X}_k retrieves features from the portion of f not already captured by earlier scales, using the stored indices from downsampling. This ensures that later scales focus on complementary information rather than duplicating what has already been encoded. The resulting features are then used for multi-scale VQVAE codebook training.

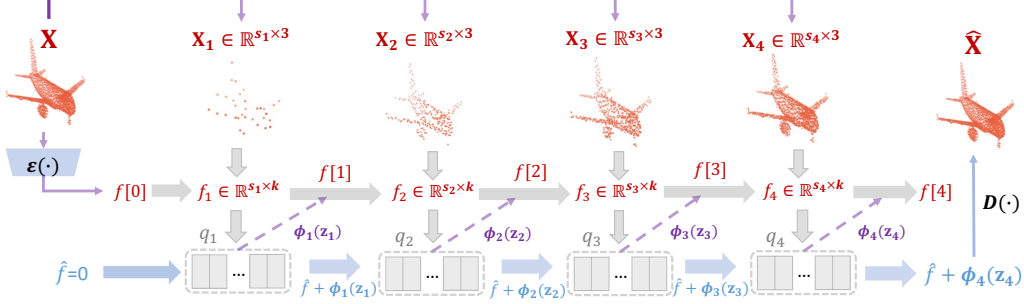


Figure 3: Illustration of training a multi-scale VQ-VAE for 3D point cloud reconstruction across scales s_1 to s_4 , resulting in a multi-scale token sequence $Q = (q_1, \dots, q_4)$.

Multi-Scale RVQ Tokenizer. We use residual vector quantization (RVQ) [57, 20] to approximate f progressively. Each residual feature f_k is quantized into tokens $q_k = \{q_k^1, q_k^2, \dots, q_k^{s_k}\} = Q(f_k) \in [V]^{s_k}$, where each q_k^i indexes the nearest codebook embedding $\mathbf{z}_v \in \mathbb{R}^d$: $q_k^i = \arg \min_{v \in [V]} \|\mathbf{z}_v - f_k^i\|_2$. This produces scale token sets q_1, \dots, q_K and corresponding embeddings $\mathbf{z}_1 \in \mathbb{R}^{s_1 \times d}, \dots, \mathbf{z}_K \in \mathbb{R}^{s_K \times d}$, which together provide a residual approximation of the original feature f as follows:

$$f_k = f_{k-1} - \phi_k(\text{upsampling}(\mathbf{z}_k, s_K)), f_0 = f \quad (4)$$

Here $\phi_k(\cdot) : \mathbb{R}^{N \times d} \rightarrow \mathbb{R}^{N \times d}$ refines the latent embedding. The $\text{upsampling}(\cdot, s_K)$ module consists of a series of reshaping operations to upsample the latent $\mathbf{z}_k \in \mathbb{R}^{s_k \times d}$ to the highest (target) resolution $s_K \times d$. Compared to the vanilla VQ [58], the above RVQ mechanism allows finer approximation of the original f with more efficient codebook utilization. We could compute the partial sum \hat{f} and reconstruct the final predicted 3D shape $\hat{\mathbf{X}}$ as follows:

$$\hat{\mathbf{X}} = D(\hat{f}), \hat{f} = \sum_{k=1}^K \phi_k(\text{upsampling}(\mathbf{z}_k, s_K)), \mathbf{z}_k = \text{lookup}(q_k), \quad (5)$$

where $D(\cdot) : \mathbb{R}^{N \times d} \rightarrow \mathbb{R}^{N \times 3}$ is a simple MLP decoder. Eq. 5 shows that $\hat{\mathbf{X}}$ is obtained by aggregating information across all scales of the level-of-detail (LoD). The pseudo-algorithms and process are illustrated in Algorithm 1, Algorithm 2, and Figure 3.

Upsampling & Reconstruction. The upsampling operation in both Eq. 4 and Eq. 5 follows a PU-Net [68] like operation, which consists of the duplicating and reshaping:

$$\mathbf{z}_k(s_k \times d) \xrightarrow{\text{duplicate}} \mathbf{z}_k(s_k \times r \times d) \xrightarrow{\text{reshape}} \mathbf{z}_k((s_k * r) \times d) = \mathbf{z}_K(s_K \times d), \quad (6)$$

where the upsampling rate $r = \frac{s_K}{s_k}$ can be pre-computed. This upsampling operation can densify points by arbitrary factors while preserving the fundamental permutation-equivariance property. The reconstruction loss function to be minimized is defined as follows:

$$\mathcal{L}_{\text{recon}} = \mathcal{L}_{\text{CD}}(\mathbf{X}, \hat{\mathbf{X}}) + \mathcal{L}_{\text{EMD}}(\mathbf{X}, \hat{\mathbf{X}}) + \sum_{k=1}^K \|f[k] - sg(\mathbf{z}_k)\|_2^2 \quad (7)$$

Here, \mathcal{L}_{CD} denotes the Chamfer Distance loss, and \mathcal{L}_{EMD} denotes the Earth-Mover Distance loss. These two terms are commonly used in prior works to measure the distance between point clouds from complementary perspectives. The stop-gradient operation, $sg[\cdot]$, ensures that the latent features f used for reconstruction remain consistent with the quantized latent vectors \mathbf{z} .

3.3 Autoregressive Transformer for Next-scale LoD Prediction

The next step is to train an autoregressive transformer on the multi-scale token sequence $Q = (q_1, \dots, q_K)$ obtained from the previous stage. Due to the strong local-geometry inductive bias inherent in 3D structures and the relatively smaller dataset size compared to 2D images, a naive causal transformer struggles to efficiently capture both intra-scale and inter-scale interactions. Consequently, it becomes necessary to embed geometric information into the transformer design, though this introduces additional challenges due to the unordered nature of point clouds.

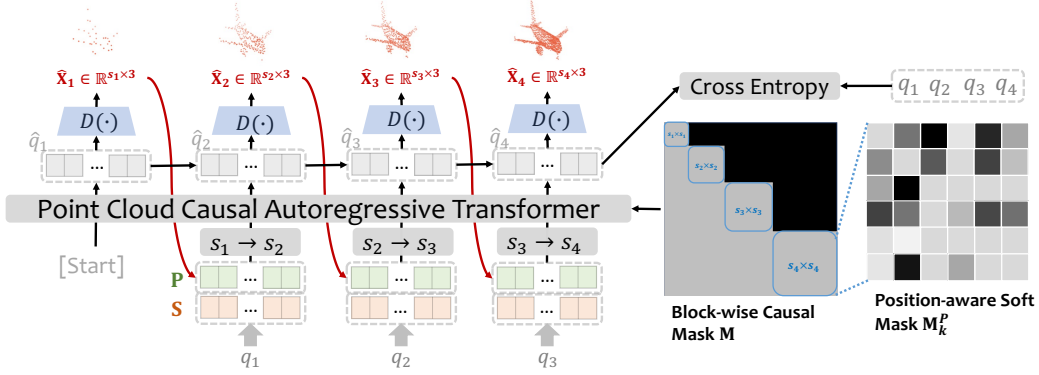


Figure 4: Illustration of training a multi-scale 3D point cloud causal transformer with intermediate decoding, upsampling, position-aware soft masks, and block-wise causal masks.

Inter-Scale Interaction Modeling. Inter-scale interactions across all scales (q_1, \dots, q_K) are essential for the model to capture relationships between scales and to generate the next LoD conditioned on the preceding ones. The model is guided by a key principle: *tokens at scale \hat{q}_k are restricted to attend only to tokens from the preceding scales $\hat{q}_1, \dots, \hat{q}_{k-1}$. Within each scale, however, all tokens $q_k = (q_k^1, \dots, q_k^{s_k})$ are allowed to fully attend to one another, ensuring that the model interprets them as complete shapes at the corresponding resolution.* To enforce this constraint, we construct the causal mask \mathbf{M} as a block-diagonal matrix, where each diagonal block \mathbf{M}_k of size $s_k \times s_k$ is fully unmasked: $\mathbf{M} = \text{diag}[\mathbf{M}_1, \mathbf{M}_2, \dots, \mathbf{M}_K]$. This design allows bidirectional dependencies within each scale while preserving a lower-triangular structure across scales, thereby preventing information leakage from future tokens. To further distinguish scales, each token is assigned a scale embedding $s_k^i \in \mathbb{R}^d$, implemented as a one-hot vector over the K scales and shared among tokens within the same scale. Some algorithmic details are explained in the Appendix B.

Intra-Scale Interaction Modeling. Capturing intra-scale interactions within the token set $q_k = (q_k^1, \dots, q_k^{s_k})$ is crucial for the model to effectively understand shapes across different resolutions. An important geometric prior is the relative distance between pairs of point tokens. Incorporating this information into intra-scale bidirectional attention allows tokens to place greater weight on nearby neighbors rather than starting from uniform attention. Specifically, we compute the position-aware soft masking matrix $\mathbf{M}_k^p \in \mathbb{R}^{s_k \times s_k}$, which is derived from the coordinate-based positional embedding matrix $\mathbf{P}_k \in \mathbb{R}^{s_k \times d}$, as follows:

$$\mathbf{M}_k^p = \text{Softmax}((\mathbf{P}_k \mathbf{W}_p)(\mathbf{P}_k \mathbf{W}_p)^T), \quad \mathbf{W}_p \in \mathbb{R}^{d \times d}. \quad (8)$$

\mathbf{M}_k^p is a symmetric matrix, where each entry $\mathbf{M}_k^p[i, j] \in (0, 1)$ encodes the relative position between points i and j . This raises a key question: *how can we derive the positional embedding \mathbf{P}_k for each scale when no explicit 3D geometry is available at this stage?* Our solution is an intermediate-structure decoding strategy. Specifically, for each scale k , we apply the decoder $D(\cdot)$ to reconstruct the intermediate structure $\hat{\mathbf{X}}_{k-1}$ using all tokens predicted up to step $k-1$:

$$\hat{\mathbf{X}}_{k-1} = D\left(\sum_{m=1}^{k-1} \phi_m(\text{upsampling}(\hat{\mathbf{z}}_m, s_m))\right), \quad \{\hat{\mathbf{z}}_1, \dots, \hat{\mathbf{z}}_{k-1}\} = \text{lookup}(Z, \{\hat{q}_1, \dots, \hat{q}_{k-1}\}). \quad (9)$$

$\hat{\mathbf{X}}_{k-1} \in \mathbb{R}^{s_{k-1} \times 3}$ serves as the input coordinate information for the next scale k prediction. The positional embedding is derived as an absolute positional encoding based on the 3D coordinates $\hat{\mathbf{X}}_{k-1}$ using trigonometric functions (e.g. \sin and \cos). Constructing the encoding directly from 3D coordinates, rather than point indices, preserves permutation equivariance. The detailed derivation of \mathbf{P} is provided in the Appendix B. Note that any positional encoding based on token indices should not be applied, as it would violate the permutation-equivariant property.

The prediction of each token \hat{q}_k^i is evaluated using the cross-entropy (CE) loss \mathcal{L}_k^i . We first compute intra-scale loss $\mathcal{L}_k = \frac{1}{s_k} \sum_{i=1}^{s_k} \mathcal{L}_k^i$ and then compute inter-scale loss $\mathcal{L}_{\text{total}} = \frac{1}{K} \sum_{k=1}^K \mathcal{L}_k$. The second stage training architecture is illustrated in Figure 4. We provide a theoretical analysis of the permutation invariance of *PointNSP*'s distribution modeling in Appendix A.

Table 1: The *Performance* (1-NNA) is evaluated based on single-class generation. The second block specifies the types of generative models used in each study. The best performance is highlighted in **bold**, while the second-best performance is underlined. Performance is reported on two dataset splits: the top corresponds to the random split, and the bottom corresponds to the LION split.

Model	Generative Model	Airplane		Chair		Car		Mean CD ↓	Mean EMD ↓
		CD ↓	EMD ↓	CD ↓	EMD ↓	CD ↓	EMD ↓		
I-GAN [1]	GAN	87.30	93.95	68.58	83.84	66.49	88.78	74.12	88.86
PointFlow [66]	Normalizing Flow	75.68	70.74	62.84	60.57	58.10	56.25	65.54	62.52
DPF-Net [19]	Normalizing Flow	75.18	65.55	62.00	58.53	62.35	54.48	66.51	59.52
SoftFlow [17]	Normalizing Flow	76.05	65.80	59.21	60.05	64.77	60.09	66.67	61.98
SetVAE [18]	VAE	75.31	77.65	58.76	61.48	59.66	61.48	64.58	66.87
ShapeGF [2]	Diffusion	80.00	76.17	68.96	65.48	63.20	56.53	70.72	66.06
DPM [33]	Diffusion	76.42	86.91	60.05	74.77	68.89	79.97	68.45	80.55
PVD-DDIM [52]	Diffusion	76.21	69.84	61.54	57.73	60.95	59.35	66.23	62.31
PSF [62]	Diffusion	74.45	67.54	58.92	54.45	57.19	56.07	62.41	57.20
PVD [74]	Diffusion	73.82	64.81	56.26	53.32	54.55	53.83	61.54	57.32
LION [70]	Diffusion	72.99	64.21	55.67	53.82	53.47	53.21	61.75	57.59
DIT-3D [36]	Diffusion	-	-	54.58	53.21	-	-	-	-
TIGER [48]	Diffusion	73.02	64.10	55.15	53.18	53.21	53.95	60.46	57.08
PointGrow [54]	Autoregressive	82.20	78.54	63.14	61.87	67.56	65.89	70.96	68.77
CanonicalVAE [7]	Autoregressive	80.15	76.27	62.78	61.05	63.23	61.56	68.72	66.29
PointGPT [4]	Autoregressive	74.85	65.61	57.24	55.01	55.91	54.24	63.44	62.24
<i>PointNSP-s (ours)</i>	Autoregressive	72.92	63.98	54.89	53.02	52.86	52.07	60.22	56.36
<i>PointNSP-m (ours)</i>	Autoregressive	72.24	63.69	54.54	52.85	52.17	51.85	59.65	56.13
LION	Diffusion	67.41	61.23	53.70	52.34	53.41	51.14	58.17	54.90
TIGER	Diffusion	67.21	56.26	54.32	51.71	54.12	50.24	58.55	52.74
<i>PointNSP-s (ours)</i>	Autoregressive	67.15	56.12	54.22	51.19	53.98	50.15	58.45	52.49
<i>PointNSP-m (ours)</i>	Autoregressive	66.98	56.05	54.01	53.76	53.12	50.09	58.04	52.30

4 Experiments

4.1 Experimental Setup

Datasets. In line with prior studies, we use ShapeNetv2, pre-processed by PointFlow [66], as our primary dataset. Following previous experimental setups, we focus on the three categories with the largest number of samples: airplanes, chairs, and cars. Each shape is globally normalized and sampled to 2048 points. The training set comprises 2832 airplanes, 4612 chairs, and 2458 cars, while the evaluation set contains 405 airplanes, 662 chairs, and 352 cars. Experiments are conducted on two data splits inherited from LION [70] and TIGER [48].

Metrics. In line with the benchmarks established by PVD [74] and LION [70], we adopt the 1-NN (1-nearest neighbor) accuracy [30] as our evaluation criterion. This metric has demonstrated its effectiveness in assessing both the quality and diversity of the generated point clouds, with a score approaching 50% indicating exceptional performance [66]. To calculate the 1-NN distance matrix, we employ two widely recognized metrics for measuring the distance between point clouds: Chamfer Distance (CD) and Earth Movers’ Distance (EMD). We also present the mean CD and the mean EMD by calculating the average CD and EMD across three distinct categories. To assess efficiency, we evaluate the training time by documenting the GPU hours and gauge the sampling efficiency by reporting the average inference time over 10 randomly generated samples.

4.2 Performance Comparison for Single-Class Generation

Results. To evaluate the performance of *PointNSP*, we compare it against several strong baseline models. Specifically, we include state-of-the-art (SoTA) diffusion-based methods: DPM [33], PVD [74], LION [70], DIT-3D [36], and TIGER [48]. We also evaluate PVD-DDIM [52], which is designed to accelerate the sampling process of PVD. In addition, we include three leading autoregressive models: PointGrow [54], CanonicalVAE [7], and PointGPT [4]. We report results for two variants of our model—*PointNSP-s* and *PointNSP-m*—representing small and medium parameter configurations, respectively. Note that we only compare against models with publicly available code. **Quality.** As shown in Table 1, *PointNSP* consistently outperforms all baseline models on both the conventional and LION data splits, achieving state-of-the-art generation quality in terms of both CD and EMD metrics. Notably, even the lightweight *PointNSP-s* demonstrates competitive performance. **Efficiency.** Table 2 presents the training time, sampling time, and number of parameters for several

Table 2: Training time (in GPU hours, averaged over three categories), sampling time (in seconds, averaged over 10 samples), and model size (in millions of parameters). Ranked by MeanCD and MeanEMD.

Quality Rank	Model	Training Time (GPU hours) ↓	Sampling Time (s) ↓	Param (M) ↓
8	PointGrow	156	5.80	25
7	CanonicalVAE	142	5.45	30
6	PointGPT	185	5.32	46
5	PVD	142	29.9	45
4	LION	550	31.2	60
3	TIGER	164	23.6	55
2	<i>PointNSP-s (ours)</i>	125	3.21	22
1	<i>PointNSP-m (ours)</i>	178	3.59	32

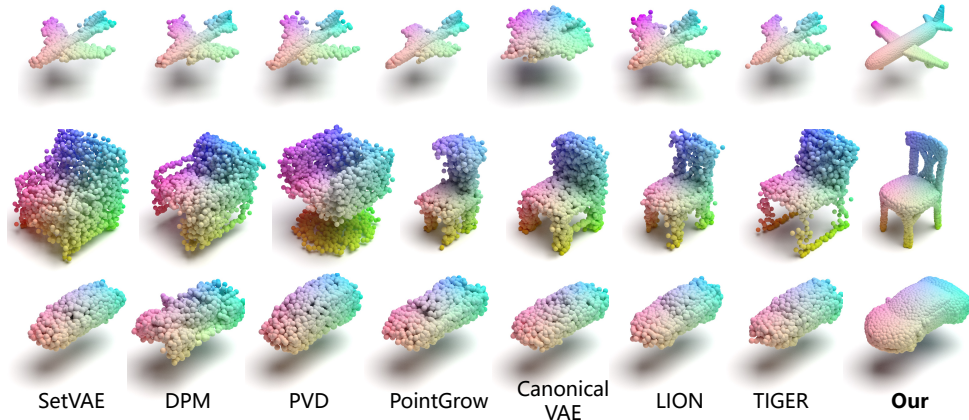


Figure 5: Our generation results (right) compared to baseline models (left). *PointNSP* generates high-quality and diverse 3D point clouds.

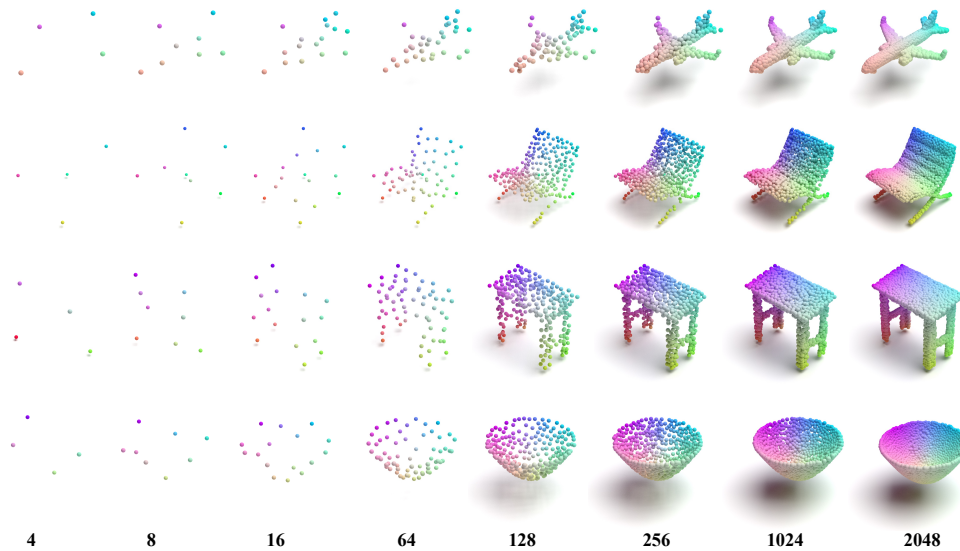


Figure 6: Visualization of multi-scale point clouds during the *PointNSP* generation process as the scale K increases.

strong baseline models from Table 1, including PVD, LION, TIGER, and PointGPT. In terms of training efficiency, *PointNSP-s* achieves the shortest training time among all selected methods, while *PointNSP-m* demonstrates comparable training costs to state-of-the-art diffusion-based approaches. For inference efficiency, both *PointNSP-s* and *PointNSP-m* outperform selected strong baseline methods with significantly faster sampling speeds. This advantage is primarily due to *PointNSP*'s parallel token generation within each scale. Additionally, *PointNSP* exhibits the highest parameter efficiency among all compared approaches. Notably, *PointNSP-s* has a smaller parameter size than PointGrow, despite the latter performing significantly worse in generation quality. Compared to diffusion-based methods, *PointNSP-m* offers a substantial advantage in parameter efficiency, requiring nearly half the number of parameters while maintaining superior performance.

4.3 Ablation and Analysis

Neural Architectures & Training Strategies We conduct comprehensive ablation studies to assess the impact of various architectural components and training strategies. First, we compare two upsampling strategies: *voxel-based representations* and *PU-Net*. Our experiments show that PU-Net consistently outperforms voxel-based upsampling, owing to its permutation-equivariant design. Second, we evaluate the effectiveness of the *position-aware masking strategy*, which significantly

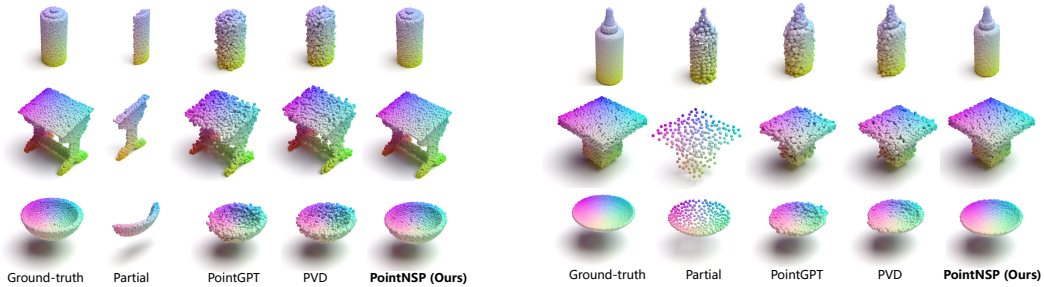


Figure 7: (Left) Visualizations of point cloud completion results. (Right) Visualizations of point cloud upsampling results.

Table 3: Ablation studies on the Transformer backbones, upsampling networks, token embedding, and FPS stochasticity.

Mask	Upsampling		FPS Stochasticity	TE	Mean CD ↓	Mean EMD ↓
	Voxel	PU-Net				
				SE	64.25	60.53
✓		✓		SE+A-PE	62.19	58.23
✓	✓			SE+A-PE	63.05	58.47
✓		✓		L-PE	63.22	59.71
✓		✓		A-PE	62.12	60.02
✓		✓		A-PE	61.28	57.32
✓		✓	✓	SE+L-PE	60.62	57.34
✓	✓	✓	✓	SE+A-PE	59.65	56.13

Table 4: Multi-Class Generation results (1-NNA↓) on ShapeNet dataset from PointFlow. All data normalized individually into [-1, 1].

	Airplane		Chair		Car	
	CD ↓	EMD ↓	CD ↓	EMD ↓	CD ↓	EMD ↓
PVD	97.53	99.88	88.37	96.37	89.77	94.89
TIGER	83.54	81.55	57.34	61.45	63.79	57.24
PointGPT	94.94	91.73	71.83	79.00	89.35	87.22
LION	86.30	77.04	66.50	63.85	64.52	54.21
<i>PointNSP-s (ours)</i>	78.95	68.84	58.79	55.10	59.97	52.89
<i>PointNSP-m (ours)</i>	75.42	66.54	56.03	52.22	57.95	49.55

boosts model performance. Third, we analyze the contribution of each embedding module in the token embedding (TE) layer, with results highlighting the notable impact of the scale embedding. We also compare *learnable positional encoding (L-PE)* with *absolute PE (A-PE)*, finding that absolute PE yields better performance. Finally, we investigate the effect of FPS *stochasticity*, arising from the inherent randomness of the FPS algorithm. We compare against a variant with a fixed starting point, which produces deterministic downsampling. The results demonstrate that FPS stochasticity consistently enhances model generalization. These findings are summarized in Table 3, with additional ablation results—such as the effect of varying the number of scales—provided in the Appendix C.

4.4 Multi-class Generation & Dense Point Cloud Generation

Beyond the single-class generation setting, we further evaluate all models on the more challenging multi-class generation task introduced by LION [70], aiming to assess their ability to generalize across diverse object categories. Specifically, we train *PointNSP* and all baseline models using class conditioning over 55 distinct categories from ShapeNet. This conditional setup allows the model to capture class-specific characteristics while also leveraging shared geometric patterns across categories. As shown in Table 4, *PointNSP* significantly outperforms all strong baselines. We provide visualizations of diverse shape classes in Appendix E. We further evaluate all models on high-resolution point cloud generation with up to 8192 points. Empirical results demonstrate that *PointNSP* maintains superior performance across all major metrics, with a widening performance margin as resolution increases—particularly training and inference speed (Results are shown in Table 5 (right) and the Appendix D).

4.5 Point Cloud Completion & Upsampling

We evaluate *PointNSP* on two key downstream tasks: point cloud completion and upsampling. For completion, we follow the experimental setup of PVD [74]. For upsampling, we use a factor of $r = 2$, increasing the input point clouds from 1024 to 2048 points. As shown in Table 5 (Left & Middle), *PointNSP* consistently achieves the best performance on point cloud completion. For the upsampling task, it outperforms all selected baselines across both metrics, highlighting its effectiveness on diverse downstream applications and its potential as a foundation model. Visualization results for these two tasks are presented in Figure 7 and Appendix E.

Table 5: (Left) The shape completion task in PVD; (Middle) Our own upsampling task by upsampling to denser point clouds; (Right) Denser point cloud generation with 8192 points.

Category	Model	CD ↓	EMD ↓	Category	Model	CD ↓	EMD ↓	Category	Model	CD ↓	EMD ↓
Airplane	SoftFlow	40.42	11.98	Airplane	PVD	73.56	71.65	Airplane	PVD	69.77	69.98
	PointFlow	40.30	11.80		TIGER	71.65	59.94		TIGER	68.48	60.24
	DPF-Net	52.79	11.05		PointGPT	72.11	60.12		PointGPT	69.29	61.56
	PVD	44.15	10.30		LION	70.41	59.65		LION	68.95	60.38
	PointNSP-m (ours)	40.12	10.08		PointNSP-m (ours)	68.89	58.86		PointNSP-m (ours)	66.63	55.29
Chair	SoftFlow	27.86	32.95	Chair	PVD	53.81	64.61	Chair	PVD	52.56	51.33
	PointFlow	27.07	36.49		TIGER	52.80	52.98		TIGER	51.87	51.85
	DPF-Net	27.63	33.20		PointGPT	53.75	53.21		PointGPT	52.43	52.09
	PVD	32.11	29.39		LION	53.98	54.33		LION	53.76	53.45
	PointNSP-m (ours)	27.02	28.78		PointNSP-m (ours)	52.04	51.03		PointNSP-m (ours)	50.98	50.45
Car	SoftFlow	18.50	27.89	Car	PVD	58.95	48.43	Car	PVD	54.19	46.55
	PointFlow	18.03	28.51		PointGPT	57.26	47.85		PointGPT	54.97	45.20
	DPF-Net	13.96	23.18		TIGER	57.90	48.01		TIGER	53.78	44.12
	PVD	17.74	21.46		LION	57.14	47.56		LION	54.98	44.67
	PointNSP-m (ours)	13.84	20.68		PointNSP-m (ours)	55.85	46.74		PointNSP-m (ours)	52.40	43.05

5 Conclusions

In this study, we present *PointNSP*, a novel autoregressive framework for high-quality 3D point cloud generation. Unlike prior methods, *PointNSP* adopts a coarse-to-fine strategy that captures the multi-scale LoD of 3D shapes without reducing them to sequences of local predictions, thereby preserving global structural coherence throughout generation. Our approach consistently outperforms existing point cloud generative models in quality while delivering significant improvements in parameter efficiency, training efficiency, and inference speed. Looking ahead, we plan to scale *PointNSP* toward foundation-level models on large datasets and explore its integration with diffusion-based approaches as a promising future direction.

References

- [1] Panos Achlioptas, Olga Diamanti, Ioannis Mitliagkas, and Leonidas J. Guibas. Learning representations and generative models for 3d point clouds. In *Proceedings of the 35th International Conference on Machine Learning, ICML 2018, Stockholm, Sweden, July 10-15, 2018*, volume 80 of *Proceedings of Machine Learning Research*, pages 40–49. PMLR, 2018.
- [2] Ruojin Cai, Guandao Yang, Hadar Averbuch-Elor, Zekun Hao, Serge J. Belongie, Noah Snavely, and Bharath Hariharan. Learning gradient fields for shape generation. In *Computer Vision - ECCV 2020 - 16th European Conference, Glasgow, UK, August 23-28, 2020, Proceedings, Part III*, volume 12348 of *Lecture Notes in Computer Science*, pages 364–381. Springer, 2020.
- [3] Huiwen Chang, Han Zhang, Lu Jiang, Ce Liu, and William T. Freeman. Maskgit: Masked generative image transformer. In *IEEE/CVF Conference on Computer Vision and Pattern Recognition, CVPR 2022, New Orleans, LA, USA, June 18-24, 2022*, pages 11305–11315. IEEE, 2022.
- [4] Guangyan Chen, Meiling Wang, Yi Yang, Kai Yu, Li Yuan, and Yufeng Yue. Pointgpt: Autoregressively generative pre-training from point clouds. In *Advances in Neural Information Processing Systems 36: Annual Conference on Neural Information Processing Systems 2023, NeurIPS 2023, New Orleans, LA, USA, December 10 - 16, 2023*, 2023.
- [5] Tian Qi Chen, Yulia Rubanova, Jesse Bettencourt, and David Duvenaud. Neural ordinary differential equations. In *Advances in Neural Information Processing Systems 31: Annual Conference on Neural Information Processing Systems 2018, NeurIPS 2018, December 3-8, 2018, Montréal, Canada*, pages 6572–6583, 2018.
- [6] Yongwei Chen, Yushi Lan, Shangchen Zhou, Tengfei Wang, and Xingang Pan. SAR3D: autoregressive 3d object generation and understanding via multi-scale 3d VQVAE. In *IEEE/CVF Conference on Computer Vision and Pattern Recognition, CVPR 2025, Nashville, TN, USA, June 11-15, 2025*, pages 28371–28382. Computer Vision Foundation / IEEE, 2025.
- [7] An-Chieh Cheng, Xueting Li, Sifei Liu, Min Sun, and Ming-Hsuan Yang. Autoregressive 3d shape generation via canonical mapping. In *Computer Vision - ECCV 2022 - 17th European Conference, Tel Aviv, Israel, October 23-27, 2022, Proceedings, Part III*, volume 13663 of *Lecture Notes in Computer Science*, pages 89–104. Springer, 2022.

- [8] Alexey Dosovitskiy, Lucas Beyer, Alexander Kolesnikov, Dirk Weissenborn, Xiaohua Zhai, Thomas Unterthiner, Mostafa Dehghani, Matthias Minderer, Georg Heigold, Sylvain Gelly, Jakob Uszkoreit, and Neil Houlsby. An image is worth 16x16 words: Transformers for image recognition at scale. In *9th International Conference on Learning Representations, ICLR 2021, Virtual Event, Austria, May 3-7, 2021*. OpenReview.net, 2021.
- [9] Hang Du, Xuejun Yan, Jingjing Wang, Di Xie, and Shiliang Pu. Point cloud upsampling via cascaded refinement network. In *Computer Vision - ACCV 2022 - 16th Asian Conference on Computer Vision, Macao, China, December 4-8, 2022, Proceedings, Part I*, volume 13841 of *Lecture Notes in Computer Science*, pages 106–122. Springer, 2022.
- [10] Abhimanyu Dubey, Abhinav Jauhri, Abhinav Pandey, Abhishek Kadian, Ahmad Al-Dahle, Aiesha Letman, Akhil Mathur, Alan Schelten, Amy Yang, Angela Fan, Anirudh Goyal, Anthony Hartshorn, Aobo Yang, Archi Mitra, Archie Sravankumar, Artem Korenev, Arthur Hinsvark, Arun Rao, Aston Zhang, Aurélien Rodriguez, Austen Gregerson, Ava Spataru, Baptiste Rozière, Bethany Biron, Binh Tang, Bobbie Chern, Charlotte Caucheteux, Chaya Nayak, Chloe Bi, Chris Marra, Chris McConnell, Christian Keller, Christophe Touret, Chunyang Wu, Corinne Wong, Cristian Canton Ferrer, Cyrus Nikolaidis, Damien Allonsius, Daniel Song, Danielle Pintz, Danny Livshits, David Esibou, Dhruv Choudhary, Dhruv Mahajan, Diego Garcia-Olano, Diego Perino, Dieuwke Hupkes, Egor Lakomkin, Ehab AlBadawy, Elina Lobanova, Emily Dinan, Eric Michael Smith, Filip Radenovic, Frank Zhang, Gabriel Synnaeve, Gabrielle Lee, Georgia Lewis Anderson, Graeme Nail, Grégoire Mialon, Guan Pang, Guillem Cucurell, Hailey Nguyen, Hannah Korevaar, Hu Xu, Hugo Touvron, Iliyan Zarov, Imanol Arrieta Ibarra, Isabel M. Kloumann, Ishan Misra, Ivan Evtimov, Jade Copet, Jaewon Lee, Jan Geffert, Jana Vranes, Jason Park, Jay Mahadeokar, Jeet Shah, Jelmer van der Linde, Jennifer Billock, Jenny Hong, Jenya Lee, Jeremy Fu, Jianfeng Chi, Jianyu Huang, Jiawen Liu, Jie Wang, Jiecao Yu, Joanna Bitton, Joe Spisak, Jongsoo Park, Joseph Rocca, Joshua Johnstun, Joshua Saxe, Junteng Jia, Kalyan Vasuden Alwala, Kartikeya Upasani, Kate Plawiak, Ke Li, Kenneth Heafield, Kevin Stone, and et al. The llama 3 herd of models. *CoRR*, abs/2407.21783, 2024.
- [11] Yuval Eldar, Michael Lindenbaum, Moshe Porat, and Yehoshua Y. Zeevi. The farthest point strategy for progressive image sampling. *IEEE Trans. Image Process.*, 6(9):1305–1315, 1997.
- [12] Patrick Esser, Robin Rombach, and Björn Ommer. Taming transformers for high-resolution image synthesis. In *IEEE Conference on Computer Vision and Pattern Recognition, CVPR 2021, virtual, June 19-25, 2021*, pages 12873–12883. Computer Vision Foundation / IEEE, 2021.
- [13] Wanquan Feng, Jin Li, Hongrui Cai, Xiaonan Luo, and Juyong Zhang. Neural points: Point cloud representation with neural fields for arbitrary upsampling. In *IEEE/CVF Conference on Computer Vision and Pattern Recognition, CVPR 2022, New Orleans, LA, USA, June 18-24, 2022*, pages 18612–18621. IEEE, 2022.
- [14] Will Grathwohl, Ricky T. Q. Chen, Jesse Bettencourt, Ilya Sutskever, and David Duvenaud. FFJORD: free-form continuous dynamics for scalable reversible generative models. In *7th International Conference on Learning Representations, ICLR 2019, New Orleans, LA, USA, May 6-9, 2019*. OpenReview.net, 2019.
- [15] Yun He, Danhang Tang, Yinda Zhang, Xiangyang Xue, and Yanwei Fu. Grad-pu: Arbitrary-scale point cloud upsampling via gradient descent with learned distance functions. In *IEEE/CVF Conference on Computer Vision and Pattern Recognition, CVPR 2023, Vancouver, BC, Canada, June 17-24, 2023*, pages 5354–5363. IEEE, 2023.
- [16] Jonathan Ho, Ajay Jain, and Pieter Abbeel. Denoising diffusion probabilistic models. In Hugo Larochelle, Marc’Aurelio Ranzato, Raia Hadsell, Maria-Florina Balcan, and Hsuan-Tien Lin, editors, *Advances in Neural Information Processing Systems 33: Annual Conference on Neural Information Processing Systems 2020, NeurIPS 2020, December 6-12, 2020, virtual*, 2020. URL <https://proceedings.neurips.cc/paper/2020/hash/4c5bcfec8584af0d967f1ab10179ca4b-Abstract.html>.
- [17] Hyeongju Kim, Hyeonseung Lee, Woo Hyun Kang, Joun Yeop Lee, and Nam Soo Kim. Softflow: Probabilistic framework for normalizing flow on manifolds. In *Advances in Neural Information Processing Systems 33: Annual Conference on Neural Information Processing Systems 2020, NeurIPS 2020, December 6-12, 2020, virtual*, 2020.

- [18] Jinwoo Kim, Jaehoon Yoo, Juho Lee, and Seunghoon Hong. Setvae: Learning hierarchical composition for generative modeling of set-structured data. In *IEEE Conference on Computer Vision and Pattern Recognition, CVPR 2021, virtual, June 19-25, 2021*, pages 15059–15068. Computer Vision Foundation / IEEE, 2021.
- [19] Roman Klokov, Edmond Boyer, and Jakob Verbeek. Discrete point flow networks for efficient point cloud generation. In *Computer Vision - ECCV 2020 - 16th European Conference, Glasgow, UK, August 23-28, 2020, Proceedings, Part XXIII*, volume 12368 of *Lecture Notes in Computer Science*, pages 694–710. Springer, 2020.
- [20] Doyup Lee, Chiheon Kim, Saehoon Kim, Minsu Cho, and Wook-Shin Han. Autoregressive image generation using residual quantization. In *IEEE/CVF Conference on Computer Vision and Pattern Recognition, CVPR 2022, New Orleans, LA, USA, June 18-24, 2022*, pages 11513–11522. IEEE, 2022.
- [21] Jiabao Lei, Kewei Shi, Zhihao Liang, and Kui Jia. Armesh: Autoregressive mesh generation via next-level-of-detail prediction, 2025. URL <https://arxiv.org/abs/2509.20824>.
- [22] Ruihui Li, Xianzhi Li, Chi-Wing Fu, Daniel Cohen-Or, and Pheng-Ann Heng. PU-GAN: A point cloud upsampling adversarial network. In *2019 IEEE/CVF International Conference on Computer Vision, ICCV 2019, Seoul, Korea (South), October 27 - November 2, 2019*, pages 7202–7211. IEEE, 2019.
- [23] Ruihui Li, Xianzhi Li, Pheng-Ann Heng, and Chi-Wing Fu. Point cloud upsampling via disentangled refinement. In *IEEE Conference on Computer Vision and Pattern Recognition, CVPR 2021, virtual, June 19-25, 2021*, pages 344–353. Computer Vision Foundation / IEEE, 2021.
- [24] Tianhong Li, Yonglong Tian, He Li, Mingyang Deng, and Kaiming He. Autoregressive image generation without vector quantization. *CoRR*, abs/2406.11838, 2024.
- [25] Zeming Lin, Halil Akin, Roshan Rao, Brian Hie, Zhongkai Zhu, Wenting Lu, Nikita Smetanin, Robert Verkuil, Ori Kabeli, Yaniv Shmueli, Allan dos Santos Costa, Maryam Fazel-Zarandi, Tom Sercu, Salvatore Candido, and Alexander Rives. Evolutionary-scale prediction of atomic level protein structure with a language model. *bioRxiv*, 2022. doi: 10.1101/2022.07.20.500902.
- [26] Yaron Lipman, Ricky T. Q. Chen, Heli Ben-Hamu, Maximilian Nickel, and Matthew Le. Flow matching for generative modeling. In *The Eleventh International Conference on Learning Representations, ICLR 2023, Kigali, Rwanda, May 1-5, 2023*. OpenReview.net, 2023.
- [27] Hao Liu, Hui Yuan, Junhui Hou, Raouf Hamzaoui, and Wei Gao. PUFA-GAN: A frequency-aware generative adversarial network for 3d point cloud upsampling. *IEEE Trans. Image Process.*, 31:7389–7402, 2022.
- [28] Xingchao Liu, Chengyue Gong, and Qiang Liu. Flow straight and fast: Learning to generate and transfer data with rectified flow. In *The Eleventh International Conference on Learning Representations, ICLR 2023, Kigali, Rwanda, May 1-5, 2023*. OpenReview.net, 2023.
- [29] Zhijian Liu, Haotian Tang, Yujun Lin, and Song Han. Point-voxel CNN for efficient 3d deep learning. In *Advances in Neural Information Processing Systems 32: Annual Conference on Neural Information Processing Systems 2019, NeurIPS 2019, December 8-14, 2019, Vancouver, BC, Canada*, pages 963–973, 2019.
- [30] David Lopez-Paz and Maxime Oquab. Revisiting classifier two-sample tests. In *5th International Conference on Learning Representations, ICLR 2017, Toulon, France, April 24-26, 2017, Conference Track Proceedings*. OpenReview.net, 2017.
- [31] David Luebke, Martin Reddy, Jonathan D. Cohen, Amitabh Varshney, Benjamin Watson, and Robert Huebner. Level of detail for 3d graphics. In *level of detail for 3d graphics*. Morgan Kaufmann, San Francisco, 2003.

- [32] Luqing Luo, Lulu Tang, Wanyi Zhou, Shizheng Wang, and Zhi-Xin Yang. PU-EVA: an edge-vector based approximation solution for flexible-scale point cloud upsampling. In *2021 IEEE/CVF International Conference on Computer Vision, ICCV 2021, Montreal, QC, Canada, October 10-17, 2021*, pages 16188–16197. IEEE, 2021.
- [33] Shitong Luo and Wei Hu. Diffusion probabilistic models for 3d point cloud generation. In *IEEE Conference on Computer Vision and Pattern Recognition, CVPR 2021, virtual, June 19-25, 2021*, pages 2837–2845. Computer Vision Foundation / IEEE, 2021.
- [34] Ali Madani, Ben Krause, Eric R. Greene, Subu Subramanian, Benjamin P. Mohr, James M. Holton, Jose Luis Olmos, Caiming Xiong, Zachary Z Sun, Richard Socher, James S. Fraser, and Nikhil Vijay Naik. Large language models generate functional protein sequences across diverse families. *Nature Biotechnology*, pages 1–8, 2023. URL <https://api.semanticscholar.org/CorpusID:256304602>.
- [35] Paritosh Mittal, Yen-Chi Cheng, Maneesh Singh, and Shubham Tulsiani. Autosdf: Shape priors for 3d completion, reconstruction and generation. In *IEEE/CVF Conference on Computer Vision and Pattern Recognition, CVPR 2022, New Orleans, LA, USA, June 18-24, 2022*, pages 306–315. IEEE, 2022.
- [36] Shentong Mo, Enze Xie, Ruihang Chu, Lanqing Hong, Matthias Nießner, and Zhenguo Li. Dit-3d: Exploring plain diffusion transformers for 3d shape generation. In *Advances in Neural Information Processing Systems 36: Annual Conference on Neural Information Processing Systems 2023, NeurIPS 2023, New Orleans, LA, USA, December 10 - 16, 2023*, 2023.
- [37] OpenAI. GPT-4 technical report. *CoRR*, abs/2303.08774, 2023.
- [38] OpenAI. 2024. URL <https://openai.com/index/hello-gpt-4o/>.
- [39] Ajay Patel, Bryan Li, Mohammad Sadegh Rasooli, Noah Constant, Colin Raffel, and Chris Callison-Burch. Bidirectional language models are also few-shot learners. In *The Eleventh International Conference on Learning Representations, ICLR 2023, Kigali, Rwanda, May 1-5, 2023*. OpenReview.net, 2023.
- [40] Charles Ruizhongtai Qi, Hao Su, Kaichun Mo, and Leonidas J. Guibas. Pointnet: Deep learning on point sets for 3d classification and segmentation. In *2017 IEEE Conference on Computer Vision and Pattern Recognition, CVPR 2017, Honolulu, HI, USA, July 21-26, 2017*, pages 77–85. IEEE Computer Society, 2017.
- [41] Charles Ruizhongtai Qi, Li Yi, Hao Su, and Leonidas J. Guibas. Pointnet++: Deep hierarchical feature learning on point sets in a metric space. In *Advances in Neural Information Processing Systems 30: Annual Conference on Neural Information Processing Systems 2017, December 4-9, 2017, Long Beach, CA, USA*, pages 5099–5108, 2017.
- [42] Guocheng Qian, Abdullellah Abualshour, Guohao Li, Ali K. Thabet, and Bernard Ghanem. PU-GCN: point cloud upsampling using graph convolutional networks. In *IEEE Conference on Computer Vision and Pattern Recognition, CVPR 2021, virtual, June 19-25, 2021*, pages 11683–11692. Computer Vision Foundation / IEEE, 2021.
- [43] Guocheng Qian, Yuchen Li, Houwen Peng, Jinjie Mai, Hasan Hammoud, Mohamed Elhoseiny, and Bernard Ghanem. Pointnext: Revisiting pointnet++ with improved training and scaling strategies. In *Advances in Neural Information Processing Systems 35: Annual Conference on Neural Information Processing Systems 2022, NeurIPS 2022, New Orleans, LA, USA, November 28 - December 9, 2022*, 2022.
- [44] Yue Qian, Junhui Hou, Sam Kwong, and Ying He. Pugeo-net: A geometry-centric network for 3d point cloud upsampling. In *Computer Vision - ECCV 2020 - 16th European Conference, Glasgow, UK, August 23-28, 2020, Proceedings, Part XIX*, volume 12364 of *Lecture Notes in Computer Science*, pages 752–769. Springer, 2020.
- [45] Yue Qian, Junhui Hou, Sam Kwong, and Ying He. Deep magnification-flexible upsampling over 3d point clouds. *IEEE Trans. Image Process.*, 30:8354–8367, 2021.

- [46] Shi Qiu, Saeed Anwar, and Nick Barnes. Pu-transformer: Point cloud upsampling transformer. In *Computer Vision - ACCV 2022 - 16th Asian Conference on Computer Vision, Macao, China, December 4-8, 2022, Proceedings, Part I*, volume 13841 of *Lecture Notes in Computer Science*, pages 326–343. Springer, 2022.
- [47] Wentao Qu, Yuantian Shao, Lingwu Meng, Xiaoshui Huang, and Liang Xiao. A conditional denoising diffusion probabilistic model for point cloud upsampling. In *IEEE/CVF Conference on Computer Vision and Pattern Recognition, CVPR 2024, Seattle, WA, USA, June 16-22, 2024*, pages 20786–20795. IEEE, 2024.
- [48] Zhiyuan Ren, Minchul Kim, Feng Liu, and Xiaoming Liu. TIGER: time-varying denoising model for 3d point cloud generation with diffusion process. In *IEEE/CVF Conference on Computer Vision and Pattern Recognition, CVPR 2024, Seattle, WA, USA, June 16-22, 2024*, pages 9462–9471. IEEE, 2024.
- [49] Danilo Jimenez Rezende and Shakir Mohamed. Variational inference with normalizing flows. In *Proceedings of the 32nd International Conference on Machine Learning, ICML 2015, Lille, France, 6-11 July 2015*, volume 37 of *JMLR Workshop and Conference Proceedings*, pages 1530–1538. JMLR.org, 2015.
- [50] Philippe Schwaller, Teodoro Laino, Théophile Gaudin, Peter Bolgar, Christopher A. Hunter, Costas Bekas, and Alpha A. Lee. Molecular transformer: A model for uncertainty-calibrated chemical reaction prediction. *ACS Central Science*, 5(9):1572–1583, 2019.
- [51] Chence Shi, Minkai Xu, Zhaocheng Zhu, Weinan Zhang, Ming Zhang, and Jian Tang. Graphaf: a flow-based autoregressive model for molecular graph generation. In *8th International Conference on Learning Representations, ICLR 2020, Addis Ababa, Ethiopia, April 26-30, 2020*. OpenReview.net, 2020.
- [52] Jiaming Song, Chenlin Meng, and Stefano Ermon. Denoising diffusion implicit models. In *9th International Conference on Learning Representations, ICLR 2021, Virtual Event, Austria, May 3-7, 2021*. OpenReview.net, 2021.
- [53] Yang Song, Jascha Sohl-Dickstein, Diederik P. Kingma, Abhishek Kumar, Stefano Ermon, and Ben Poole. Score-based generative modeling through stochastic differential equations. In *9th International Conference on Learning Representations, ICLR 2021, Virtual Event, Austria, May 3-7, 2021*. OpenReview.net, 2021.
- [54] Yongbin Sun, Yue Wang, Ziwei Liu, Joshua E. Siegel, and Sanjay E. Sarma. Pointgrow: Autoregressively learned point cloud generation with self-attention. In *IEEE Winter Conference on Applications of Computer Vision, WACV 2020, Snowmass Village, CO, USA, March 1-5, 2020*, pages 61–70. IEEE, 2020.
- [55] Ilya Sutskever, Oriol Vinyals, and Quoc V. Le. Sequence to sequence learning with neural networks. In *Advances in Neural Information Processing Systems 27: Annual Conference on Neural Information Processing Systems 2014, December 8-13 2014, Montreal, Quebec, Canada*, pages 3104–3112, 2014.
- [56] Chameleon Team. Chameleon: Mixed-modal early-fusion foundation models. *CoRR*, abs/2405.09818, 2024.
- [57] Keyu Tian, Yi Jiang, Zehuan Yuan, Bingyue Peng, and Liwei Wang. Visual autoregressive modeling: Scalable image generation via next-scale prediction. *CoRR*, abs/2404.02905, 2024.
- [58] Aaron van den Oord, Oriol Vinyals, and koray kavukcuoglu. Neural discrete representation learning. In I. Guyon, U. Von Luxburg, S. Bengio, H. Wallach, R. Fergus, S. Vishwanathan, and R. Garnett, editors, *Advances in Neural Information Processing Systems*, volume 30. Curran Associates, Inc., 2017. URL https://proceedings.neurips.cc/paper_files/paper/2017/file/7a98af17e63a0ac09ce2e96d03992fbc-Paper.pdf.
- [59] Jionghao Wang, Cheng Lin, Yuan Liu, Rui Xu, Zhiyang Dou, Xiaoxiao Long, Haoxiang Guo, Taku Komura, Wenping Wang, and Xin Li. Pdt: Point distribution transformation with diffusion models. In *Proceedings of the Special Interest Group on Computer Graphics and Interactive Techniques Conference Papers*, pages 1–11, 2025.

- [60] Dirk Weissenborn, Oscar Täckström, and Jakob Uszkoreit. Scaling autoregressive video models. In *8th International Conference on Learning Representations, ICLR 2020, Addis Ababa, Ethiopia, April 26-30, 2020*. OpenReview.net, 2020.
- [61] Haibin Wu, Kai-Wei Chang, Yuan-Kuei Wu, and Hung-yi Lee. Speechgen: Unlocking the generative power of speech language models with prompts. *CoRR*, abs/2306.02207, 2023.
- [62] Lemeng Wu, Dilin Wang, Chengyue Gong, Xingchao Liu, Yunyang Xiong, Rakesh Ranjan, Raghuraman Krishnamoorthi, Vikas Chandra, and Qiang Liu. Fast point cloud generation with straight flows. In *IEEE/CVF Conference on Computer Vision and Pattern Recognition, CVPR 2023, Vancouver, BC, Canada, June 17-24, 2023*, pages 9445–9454. IEEE, 2023.
- [63] Xiaoyang Wu, Yixing Lao, Li Jiang, Xihui Liu, and Hengshuang Zhao. Point transformer V2: grouped vector attention and partition-based pooling. In *Advances in Neural Information Processing Systems 35: Annual Conference on Neural Information Processing Systems 2022, NeurIPS 2022, New Orleans, LA, USA, November 28 - December 9, 2022*, 2022.
- [64] Xiaoyang Wu, Li Jiang, Peng-Shuai Wang, Zhijian Liu, Xihui Liu, Yu Qiao, Wanli Ouyang, Tong He, and Hengshuang Zhao. Point transformer V3: simpler, faster, stronger. In *IEEE/CVF Conference on Computer Vision and Pattern Recognition, CVPR 2024, Seattle, WA, USA, June 16-22, 2024*, pages 4840–4851. IEEE, 2024.
- [65] Xingguang Yan, Liqiang Lin, Niloy J. Mitra, Dani Lischinski, Daniel Cohen-Or, and Hui Huang. Shapeformer: Transformer-based shape completion via sparse representation. In *IEEE/CVF Conference on Computer Vision and Pattern Recognition, CVPR 2022, New Orleans, LA, USA, June 18-24, 2022*, pages 6229–6239. IEEE, 2022.
- [66] Guandao Yang, Xun Huang, Zekun Hao, Ming-Yu Liu, Serge J. Belongie, and Bharath Hariharan. Pointflow: 3d point cloud generation with continuous normalizing flows. In *2019 IEEE/CVF International Conference on Computer Vision, ICCV 2019, Seoul, Korea (South), October 27 - November 2, 2019*, pages 4540–4549. IEEE, 2019.
- [67] Jiaxuan You, Rex Ying, Xiang Ren, William L. Hamilton, and Jure Leskovec. Graphrnn: Generating realistic graphs with deep auto-regressive models. In *Proceedings of the 35th International Conference on Machine Learning, ICML 2018, Stockholm, Sweden, July 10-15, 2018*, volume 80 of *Proceedings of Machine Learning Research*, pages 5694–5703. PMLR, 2018.
- [68] Lequan Yu, Xianzhi Li, Chi-Wing Fu, Daniel Cohen-Or, and Pheng-Ann Heng. Pu-net: Point cloud upsampling network. In *2018 IEEE Conference on Computer Vision and Pattern Recognition, CVPR 2018, Salt Lake City, UT, USA, June 18-22, 2018*, pages 2790–2799. Computer Vision Foundation / IEEE Computer Society, 2018.
- [69] Manzil Zaheer, Satwik Kottur, Siamak Ravanbakhsh, Barnabás Póczos, Ruslan Salakhutdinov, and Alexander J. Smola. Deep sets. In *Advances in Neural Information Processing Systems 30: Annual Conference on Neural Information Processing Systems 2017, December 4-9, 2017, Long Beach, CA, USA*, pages 3391–3401, 2017.
- [70] Xiaohui Zeng, Arash Vahdat, Francis Williams, Zan Gojcic, Or Litany, Sanja Fidler, and Karsten Kreis. LION: latent point diffusion models for 3d shape generation. In *Advances in Neural Information Processing Systems 35: Annual Conference on Neural Information Processing Systems 2022, NeurIPS 2022, New Orleans, LA, USA, November 28 - December 9, 2022*, 2022.
- [71] Dong Zhang, Shimin Li, Xin Zhang, Jun Zhan, Pengyu Wang, Yaqian Zhou, and Xipeng Qiu. Speechgpt: Empowering large language models with intrinsic cross-modal conversational abilities. In *Findings of the Association for Computational Linguistics: EMNLP 2023, Singapore, December 6-10, 2023*, pages 15757–15773. Association for Computational Linguistics, 2023.
- [72] Hengshuang Zhao, Li Jiang, Jiaya Jia, Philip H. S. Torr, and Vladlen Koltun. Point transformer. In *2021 IEEE/CVF International Conference on Computer Vision, ICCV 2021, Montreal, QC, Canada, October 10-17, 2021*, pages 16239–16248. IEEE, 2021.

- [73] Chunting Zhou, Lili Yu, Arun Babu, Kushal Tirumala, Michihiro Yasunaga, Leonid Shamis, Jacob Kahn, Xuezhe Ma, Luke Zettlemoyer, and Omer Levy. Transfusion: Predict the next token and diffuse images with one multi-modal model, 2024.
- [74] Linqi Zhou, Yilun Du, and Jiajun Wu. 3d shape generation and completion through point-voxel diffusion. In *2021 IEEE/CVF International Conference on Computer Vision, ICCV 2021, Montreal, QC, Canada, October 10-17, 2021*, pages 5806–5815. IEEE, 2021.

Appendix

A Permutation Invariance of the Probability Distribution

Here we show why the distribution $p(\mathbf{X}_1, \mathbf{X}_2, \dots, \mathbf{X}_K) = \prod_{k=1}^K p(\mathbf{X}_k | \mathbf{X}_{k-1}, \dots, \mathbf{X}_2, \mathbf{X}_1)$ in Eq 3 preserves the permutation-invariance $p(\pi(\mathbf{x}_1, \dots, \mathbf{x}_N)) = p(\mathbf{x}_1, \dots, \mathbf{x}_N), \forall \pi \in S_N$ in Eq 2.

By definition, the joint distribution factorizes as:

$$p(\mathbf{X}_1, \mathbf{X}_2, \dots, \mathbf{X}_K) = p(\mathbf{X}_1)p(\mathbf{X}_2|\mathbf{X}_1) \dots p(\mathbf{X}_K|\mathbf{X}_1, \dots, \mathbf{X}_{K-1}). \quad (10)$$

Suppose the feature encoder and the conditional model for each scale are permutation-equivariant or permutation-invariant. Then, for any permutation π_k of points within \mathbf{X}_k :

$$p(\pi_k(\mathbf{X}_k) | \mathbf{X}_1, \dots, \mathbf{X}_{k-1}) = p(\mathbf{X}_k | \mathbf{X}_1, \dots, \mathbf{X}_{k-1}). \quad (11)$$

This holds for each $k = 1, \dots, K$.

Consider an arbitrary permutation π acting on the full set of points $\mathbf{X} = \bigcup_{k=1}^K \mathbf{X}_k$. This permutation can be decomposed into independent permutations within each scale:

$$\pi = (\pi_1, \pi_2, \dots, \pi_K), \quad \pi_k \in S_{s_k}. \quad (12)$$

Then the joint distribution under this permutation is

$$\begin{aligned} p(\pi(\mathbf{X}_1, \mathbf{X}_2, \dots, \mathbf{X}_K)) &= \prod_{k=1}^K p(\pi_k(\mathbf{X}_k) | \mathbf{X}_{k-1}, \dots, \mathbf{X}_2, \mathbf{X}_1) \\ &= \prod_{k=1}^K p(\mathbf{X}_k | \mathbf{X}_{k-1}, \dots, \mathbf{X}_2, \mathbf{X}_1) \quad (\text{by permutation invariance at each scale}) \\ &= p(\mathbf{X}_1, \mathbf{X}_2, \dots, \mathbf{X}_K) \end{aligned} \quad (13)$$

The core operations in *PointNSP*—such as the feature encoder, upsampling, and FPS—are all designed to be permutation-equivariant or permutation-invariant. As a result, the autoregressive factorization preserves permutation invariance: permuting the points within any scale does not alter the joint probability.

$$p(\pi(\mathbf{x}_1, \dots, \mathbf{x}_N)) = p(\mathbf{x}_1, \dots, \mathbf{x}_N), \forall \pi \in S_N. \quad (14)$$

B Algorithm Details

Coordinate-based Positional Encoding. We adopt the absolute positional encoding strategy purely based on 3D coordinates used in TIGER [48]. Based on our experiments, we find the Base λ Position Encoding (B λ PE) performs better and here we present its formula:

$$p = \lambda^2 * z_i + \lambda * y_i + x_i \quad (15)$$

$$\mathbf{P}_k(p, 2i) = \sin\left(\frac{p}{10000^{\frac{2i}{D}}}\right) \quad (16)$$

$$\mathbf{P}_k(p, 2i + 1) = \cos\left(\frac{p}{10000^{\frac{2i}{D}}}\right), \quad (17)$$

where $\mathbf{x}_i = (x_i, y_i, z_i) \in \mathbb{R}^3$, p is a polynomial expression with hyperparameter coefficient λ . We set $\lambda = 1000$ following the setting in TIGER [48], which means this preserves three decimal places of precision. Here $\mathbf{P}_k \in \mathbb{R}^{s_k \times D}$ denotes the positional embedding of all tokens within the scale k . In short, we apply the B λ PE embedding strategy scale-by-scale at this time.

Intra-Scale Token Embedding Layer. In this way, we derive the absolute positional encoding \mathbf{p}_k^i for each token q_k^i with predicted $\hat{\mathbf{X}}_k$. Additionally, the model needs to know which scale that each token belongs to. Therefore, \mathbf{s}_k is a simple one-hot encoding $\mathbf{s}_k = \text{one-hot}(k)$ out of total K scales. Tokens (q_k^i, q_k^j) from the same scale k share the same scale embedding \mathbf{s}_k ($\mathbf{s}_k^i = \mathbf{s}_k^j$). Following the implementation of Llama 3 [10], we add both the positional embedding \mathbf{p}_k^i and the scale embedding

\mathbf{s}_k^i to the query \mathbf{u}_k^i and key vectors \mathbf{v}_k^i derived in the attention mechanism. Then the token embedding operation for each token q_k^i is as follows:

$$\mathbf{u}_k^i = \mathbf{W}_U \mathbf{z}_k^i + \mathbf{p}_k^i + \mathbf{s}_k^i, \mathbf{v}_k^i = \mathbf{W}_V \mathbf{z}_k^i + \mathbf{p}_k^i + \mathbf{s}_k^i, \quad (18)$$

where \mathbf{W}_U and \mathbf{W}_V are projection matrices for queries and keys respectively. Then the queries and keys will be upsampled to $\mathbf{U}_k, \mathbf{V}_k = \text{upsampling}(\mathbf{U}_k, \mathbf{V}_k) \in \mathbb{R}^{s_{k+1} \times d}$ following the Eq. 6, which will be fed to the transformer for next-scale token prediction.

C Hyperparameters and Reproducibility Settings

Hyper-parameters and Reproducibility Settings. We mainly follow the setting in [70]. Specifically, we set the learning rate $3e^{-4}$ and the batch-size 32. We perform all the experiments on a workstation with Intel Xeon Gold 6154 CPU (3.00GHz) and 8 NVIDIA Tesla V100 (32GB) GPUs.

We use an AdamW optimizer with an initial learning rate of 10^{-4} for VQVAE training and 10^{-3} for autoregressive transformer training respectively. For up-sampling and completion experiments, we follow the experimental settings of PVD [74].

Hyperparameter	Value
# PVCNN layers	4
# PVCNN hidden dimension	1024
# PVCNN voxel grid size	32
# MLP layers	6
# Attention dimension	1024
# Attention head	32
Optimizer	AdamW
Weight Decay	0.01
LR Schedule	Cosine

The effect of # scales K . Figure S1 illustrates the impact of the total number of scales on the overall performance of *PointNSP*. As the number of scales increases, *PointNSP*'s performance improves accordingly. However, beyond $K = 11$ scales, no further performance gains are observed. We hypothesize that additional scales may require higher point cloud densities to be effective. Moreover, increasing the number of scales naturally leads to longer sampling times.

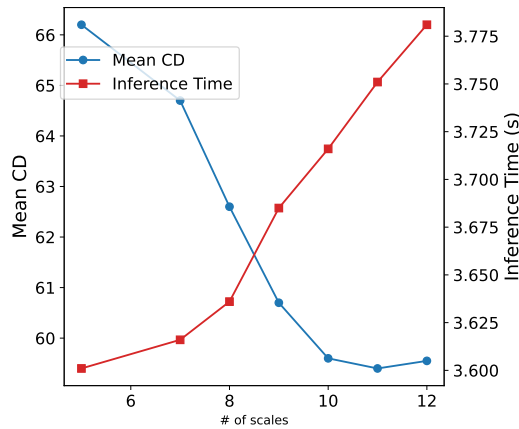


Figure S1: The effect of number of scales on the overall performance of *PointNSP*.

D More Results on Dense Point Cloud Generation with 8192 points

We show sampling time and training hours of different methods in Table S1. We could clearly see that *PointNSP* significantly outperforms other strong methods in terms of learning efficiency and inference efficiency, which shows its strong scalability potential.

Table S1: Training time (in GPU hours), sampling time (in seconds) on 8192 points. The reported training time is averaged across three categories: airplane, chair, and car. The sampling time is averaged over 10 random generations.

Quality Rank	Model	Training Time (GPU hours) ↓	Sampling Time (s) ↓
8	PointGrow	240	9.90
7	CanonicalVAE	205	8.95
6	PointGPT	296	10.56
5	PVD	201	58.1
4	LION	610	59.5
3	TIGER	320	42.1
2	<i>PointNSP-s (ours)</i>	175	4.54
1	<i>PointNSP-m (ours)</i>	190	5.48

E More Visualization Results

3D Point Clouds Generated by *PointNSP*. We showcase diverse 3D point clouds generated by *PointNSP*, covering a wide range of shapes (Figures S2 and S3). Additional results for single-class generation across five categories are presented in Figures S4–S8. We further illustrate the multi-scale sequential generation process in Figures S9–S11, and provide visualizations of point cloud completion and upsampling in Figure S12.

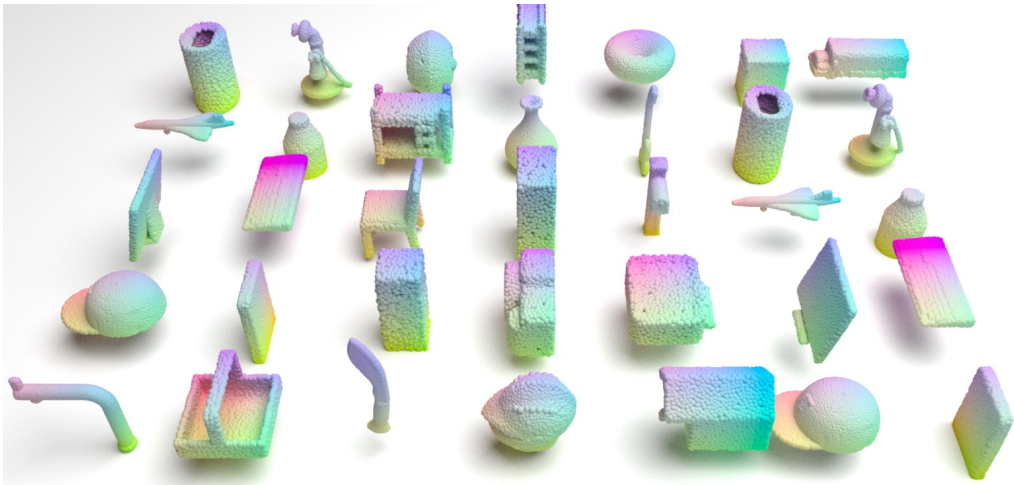


Figure S2: Generated shapes from the *PointNSP* model trained on ShapeNet’s other categories.

F Other Related Works

Point Cloud Upsampling. Point cloud upsampling is a crucial process in 3D modeling, aimed at increasing the resolution of low-resolution 3D point clouds. PU-Net [68] pioneered the use of deep neural networks for this task, laying the foundation for subsequent advancements. Models such as PU-GCN [42] and PU-Transformer [46] have further refined point cloud feature extraction by leveraging graph convolutional networks and transformer networks, respectively. Additionally, approaches like Dis-PU [23], PU-EVA [32], and MPU [9] have enhanced the PU-Net pipeline by incorporating cascading refinement architectures. Other methods, such as PUGeo-Net [44], NePs [13], and MAFU [45], employ local geometry projections into 2D space to model the underlying 3D surface. More recent approaches have reframed up-sampling as a generation task. For instance, PU-GAN [22] and PUFA-GAN [27] leverage generative adversarial networks (GANs) to produce

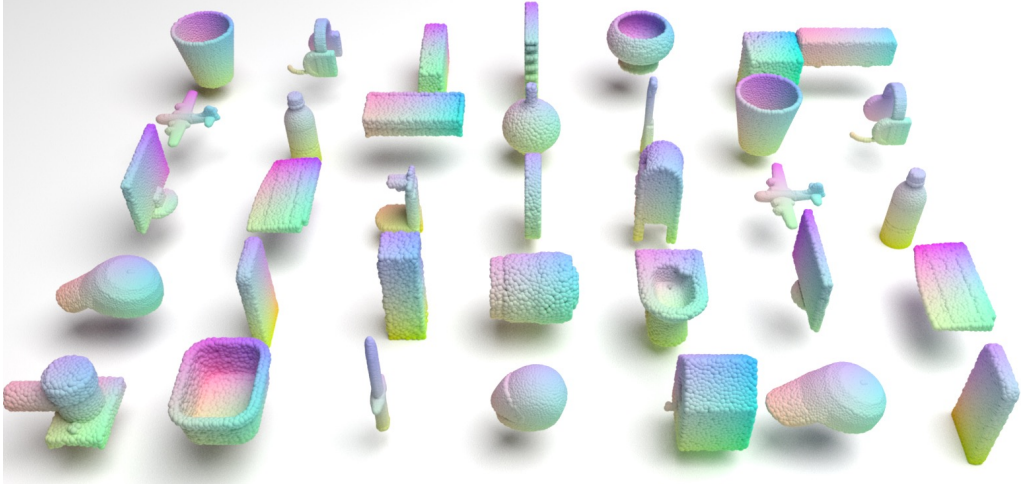


Figure S3: Generated shapes from the *PointNSP* model trained on ShapeNet’s other categories.

high-resolution point clouds. Grad-PU [15] first generates coarse dense point clouds through nearest-point interpolation and then refines them iteratively using diffusion models. In contrast, PUDM [47] directly utilizes conditional diffusion models, treating sparse point clouds as input conditions for generating denser outputs. In this work, our generative model, *PointNSP*, incorporates upsampling networks in both training stages, making it well-suited for enhancing downstream point cloud up-sampling tasks.

Autoregressive Generative Models. Autoregressive modeling has demonstrated exceptional success in natural language processing, leading to the development of powerful large language models (LLMs) such as [55, 38, 37, 39]. Building on the success of LLMs, researchers have explored autoregressive approaches across a wide range of domains, including image generation [58, 12, 24, 57, 20, 3], graph generation [67], video synthesis [60], molecule generation [51, 50], and protein sequence modeling [34, 25]. At its core, autoregressive modeling involves sequentially predicting future elements based on past outputs, making it particularly effective for audio generation tasks, where such temporal dependencies are naturally present.

G Limitations & Broader Impact

PointNSP does not present major limitations, though the main challenge lies in learning high-quality multi-scale codebook embeddings for 3D point cloud representations—a process that remains resource-intensive. Several promising directions emerge for future work. One is scaling generation to produce ultra-dense point clouds (e.g., 10k–100k points), which could then be converted into high-quality meshes. Another is enabling fine-grained control over local geometric details, an essential step toward practical applications. While this work does not pose immediate societal risks, potential misuse for generating harmful 3D content warrants vigilance from the broader community. From a research perspective, *PointNSP* makes a meaningful contribution to both generative modeling and 3D point cloud research.



Figure S4: Generated single-class shapes from the *PointNSP* model trained on ShapeNet's other categories.

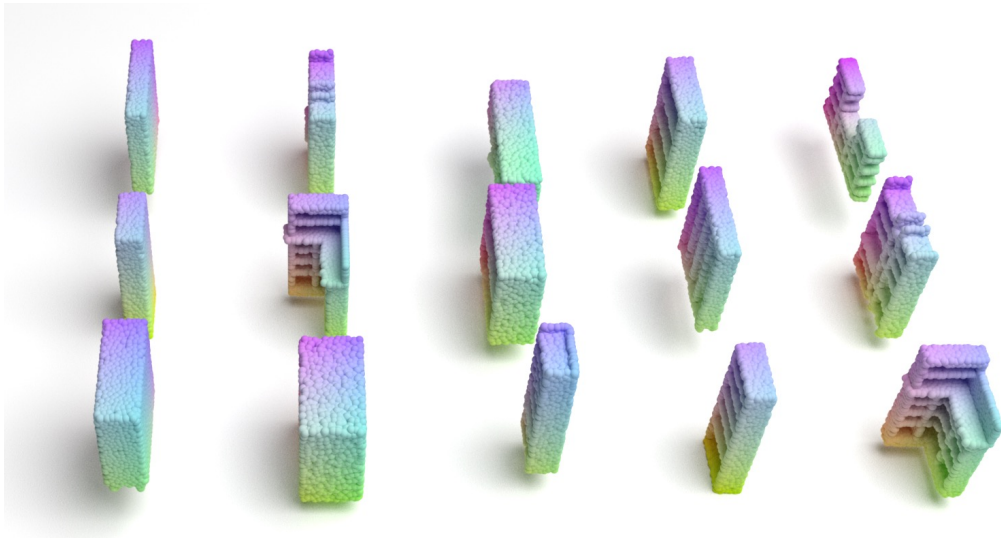


Figure S5: Generated single-class shapes from the *PointNSP* model trained on ShapeNet's other categories.

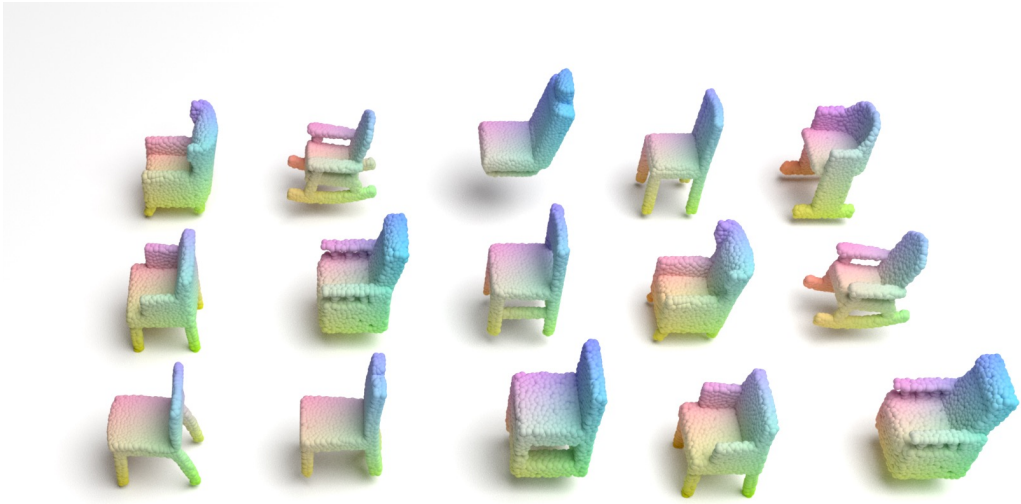


Figure S6: Generated single-class shapes from the *PointNSP* model trained on ShapeNet's other categories.



Figure S7: Generated single-class shapes from the *PointNSP* model trained on ShapeNet's other categories.

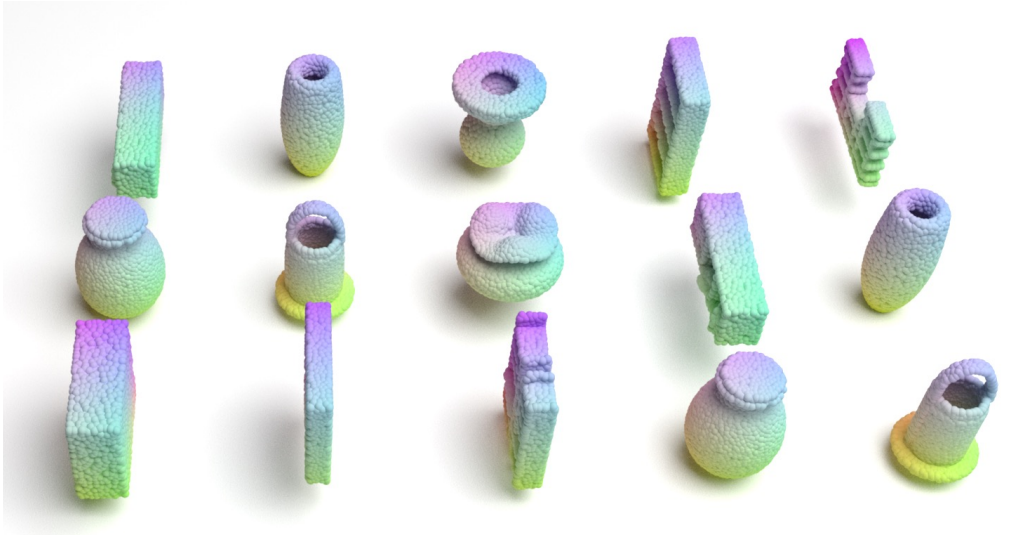


Figure S8: Generated single-class shapes from the *PointNSP* model trained on ShapeNet's other categories.

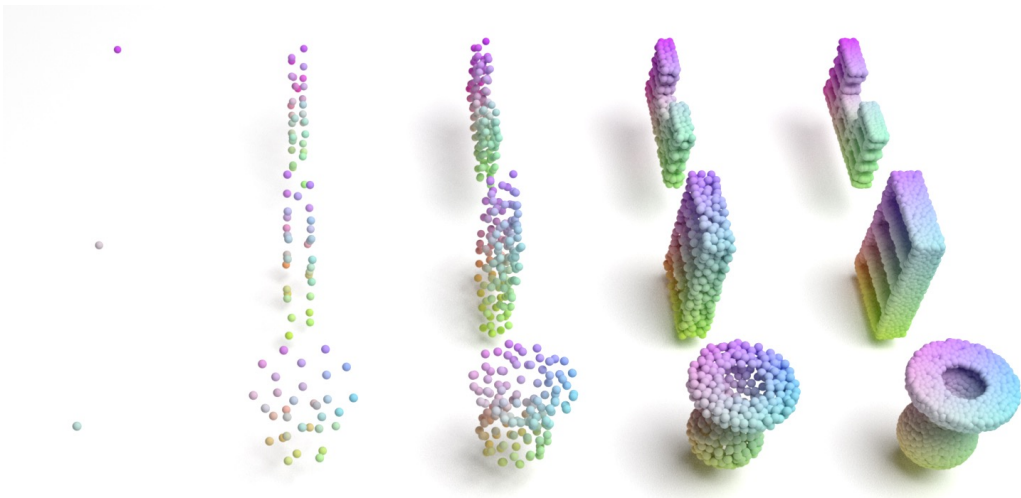


Figure S9: Illustration of multi-scale point cloud generation from the *PointNSP* model.

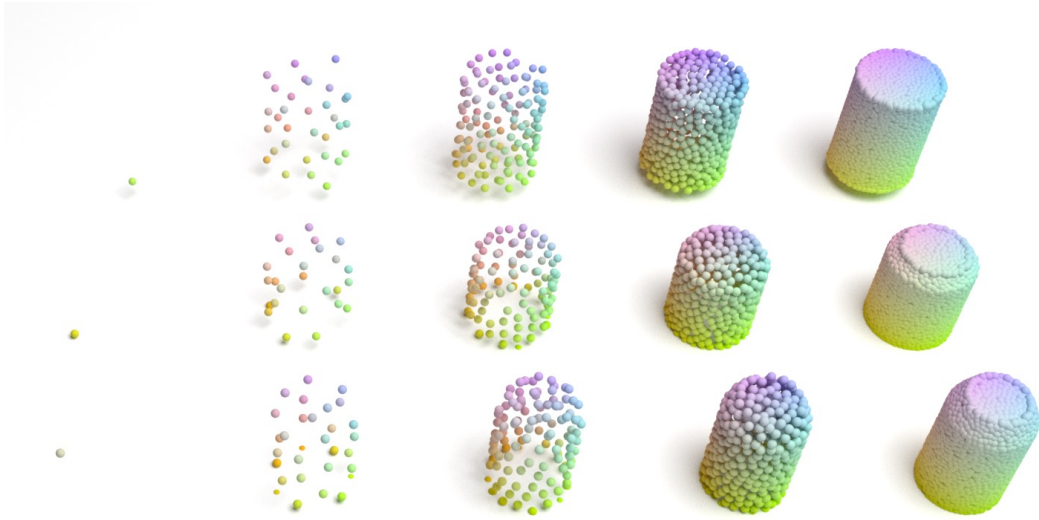


Figure S10: Illustration of multi-scale point cloud generation from the *PointNSP* model.

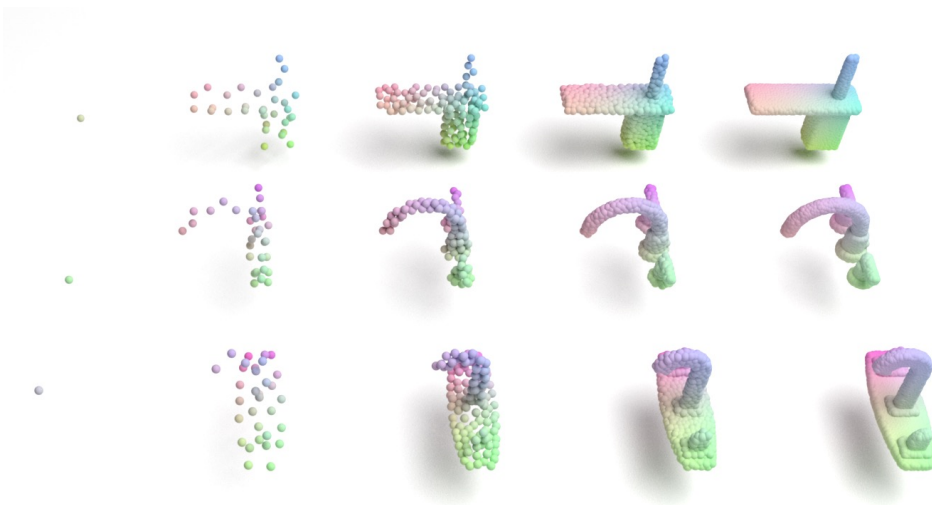


Figure S11: Illustration of multi-scale point cloud generation from the *PointNSP* model.

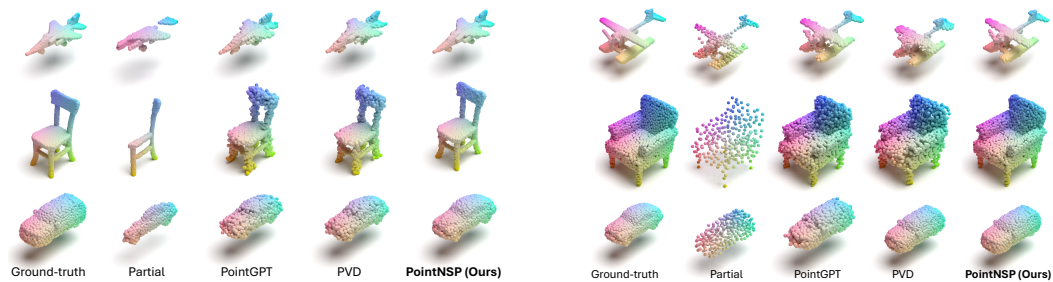


Figure S12: (Left) Visualizations of point cloud completion results. (Right) Visualizations of point cloud upsampling results.